

Inductive effects in molecular contacts enable wide-bandgap perovskite cells for efficient perovskite/TOPCon tandems

Received: 28 September 2024

Accepted: 7 May 2025

Published online: 15 May 2025



Yixin Luo^{1,9}, Yuan Tian^{1,2,9}, Ke Zhao^{1,2}, Weiping Mao³, Chen Liu⁴, Jiahui Shen^{2,4}, Zhendong Cheng², Caner Değer⁵, Xiaohu Miao⁶, Zhongwei Zhang⁷, Xuechun Sun^{1,2}, Libing Yao², Xu Zhang^{1,2}, Pengju Shi^{1,2}, Donger Jin¹, Jiaxiao Deng³, Mengyuan Tian³, İlhan Yavuz⁵, Na Dong⁷, Ruzhang Liu⁴, Rui Wang², Deren Yang¹✉ & Jingjing Xue^{1,8}✉

Organic molecules that serve as hole-selective contacts, known as self-assembled monolayers (SAMs), play a pivotal role in ensuring high-performance perovskite photovoltaics. Optimal energy alignment between the SAM and the perovskite is essential for desired photovoltaic performance. However, many SAMs are studied in optimal-bandgap perovskites, with limited energy level modification specifically catering to wide-bandgap perovskites. Herein, we demonstrate that the energy level of SAMs can be systematically tuned in a stepwise manner via inductive effects in the conjugated moieties, enabling rational design tailored for specific perovskite bandgaps. The resulting WBG perovskite device based on our tuned SAM achieved a power conversion efficiency (PCE) of 22.8%. Integration with crystalline silicon TOPCon subcells further enabled the construction of a perovskite/TOPCon tandem device with a PCE of 31.1% (certified 30.9%).

Perovskite-based tandem devices have held great promise in breaking the theoretical limit of power conversion efficiency due to their high efficiency in utilizing solar energy. With their compatibility in tandem structures, inverted wide-bandgap (WBG) perovskite semi-devices are often used as the top cell due to their absorption spectrum and thus play a crucial part in achieving high-efficiency tandems^{1–3}. A favored interfacial energetics between the charge transport layer, in particular the hole transport layer (HTL), and the wide-bandgap perovskite active layer is vital for improving the device performance. The mismatch of the interfacial energetics could induce charge accumulation and accelerated recombination, which

leads to undesired open circuit voltage (V_{oc}) loss and decreased fill factors (FF)^{4–6}.

To improve hole collection and band alignment in high-efficiency photovoltaic devices, various types of self-assembled monolayers (SAMs) have been developed^{7–10}. These molecules, due to their high structural tunability, can self-assemble into monolayer or multi-layers between the perovskite active layer and the electrode, facilitating efficient charge transport^{8,11}. Intensive researches on SAM energy levels modification primarily rely on molecular structure modifications. Based on the N-substituted π -conjugated structures and their derivatives, strategies such as backbone¹² and spacer engineering¹³,

¹State Key Laboratory of Silicon and Advanced Semiconductor Materials, School of Materials Science and Engineering, Zhejiang University, Hangzhou, China.

²School of Engineering, Westlake University and Institute of Advanced Technology, Westlake Institute for Advanced Study, Hangzhou, China. ³Jietai New Energy Technology Co., Ltd, Chuzhou City, Anhui, China. ⁴School of Chemistry and Chemical Engineering, Yangzhou University, Yangzhou, China.

⁵Department of Physics, Marmara University, Ziverbey, Istanbul, Turkey. ⁶Zhejiang Key Laboratory of Precise Synthesis of Functional Molecules, Instrumentation and Service Center for Molecular Sciences and Research Center for Industries of the Future, Westlake University, Hangzhou, China. ⁷Dongfang Electric (Hangzhou) Innovation Institute Co., Ltd., Hangzhou, China. ⁸Shangyu Institute of Semiconductor Materials, Shaoxing, China. ⁹These authors contributed equally: Yixin Luo, Yuan Tian.

✉ e-mail: mseyang@zju.edu.cn; jjxue@zju.edu.cn

heteroatom insertion and core group modification^{14,15}, anchoring group^{16,17} and functional group optimization^{8,11,18}, or mix SAM layers⁹ are employed to achieve better energy level alignment between the hole selective contact and the perovskite layer. However, current SAMs are mostly adapted from narrow-bandgap PSCs without targeted energy level tuning for WBG applications. This leads to mismatched interfacial energetics and can result in significant V_{oc} -deficit and poor hole extraction efficiency. The rational tuning of SAM energy levels to align with those of the wide-bandgap perovskite layer has yet to be fully explored.

Herein, we introduce a series of SAMs based on a fully conjugated *peri*-fused polyaromatic pyrene core, which provides a more chemically inert and structurally rigid molecular contact compared to N-substituted π -conjugated structures²⁰. The fully conjugated core group enhances the electron inductive effect within the SAMs, which refers to the local redistribution of electron density due to electron-withdrawing or electron-donating groups in the molecule^{21,22}. Such inductive effect enables precise energy level tuning of SAMs. By incorporating electron-withdrawing or electron-donating substituents, the electron density within the SAMs can be modulated to spanned over a certain range as needed, resulting in a shift of the interfacial energetics between the SAM and perovskite layer. As the SAMs self-assemble on the conductive indium tin oxide (ITO), the local change in the electron density modifies the interfacial energetics between the SAM and perovskite. The ability to adjust the inductive effects of the functional groups allows for targeted tuning of the SAM energy levels over a wide range, providing a more versatile and controlled approach to optimizing energy alignment in PSCs. Among the four molecules, the electron-donating methoxy group-modified SAM achieved a champion PCE of 22.8%, with an open V_{oc} of 1.24 V and a high FF of 84.3% for wide bandgap PSCs. The longevity of unencapsulated devices based on (E)-3-(6-methoxypyren-1-yl)acrylic acid (PyAA-MeO) retained more than 99% of the initial efficiency after 400 h of maximum power point tracking at 60 °C. More than 96% of their efficiencies were retained in different accelerated aging tests for >2500 h, demonstrating their enhanced resistance to external stimuli. Integrating the PyAA-MeO-based WBG perovskite subcells with crystalline silicon (c-Si) subcells with tunneling oxide passivating contact (TOPCon) structure, we report 31.1% (certified 30.9%) perovskite/TOPCon tandem solar cells with an active area of 1 cm², which exhibit a high FF of 82.6%, one of the highest reported efficiencies for such tandem systems.

Results

Functional groups in molecular design and influence on perovskite properties

Based on a *peri*-fused polyaromatic conjugated structure with an acrylic acid anchoring group, we designed and synthesized a series of SAMs linked with the bromine, methyl, or methoxy group, which feature different electron-withdrawing or donating capability, respectively. Apart from the conjugated pyrene core group, we further incorporated a double bond in the alkyl chain spacer to achieve a fully conjugated structure, which amplifies the inductive effect from the functional group. We designed and synthesized a series of molecules, namely (E)-3-(Pyren-1-yl)acrylic acid (PyAA), (E)-3-(6-bromopyren-1-yl)acrylic acid (PyAA-Br), (E)-3-(6-methylpyren-1-yl)acrylic acid (PyAA-Me), and (E)-3-(6-methoxypyren-1-yl)acrylic acid (PyAA-MeO). Figure 1a displays their molecular structures, see synthesis details in Supplementary Note 1-4, with molecular structures confirmed by proton and carbon nuclear magnetic resonance (¹H and ¹³C NMR) spectroscopy (Supplementary Figs. 1–20).

We deposited SAMs with different functional groups on the ITO substrate. The successful anchoring of SAMs on ITO was confirmed using X-ray photoelectron spectroscopy (XPS). The Sn 3*d* peak in the XPS pattern shifted from 495.23 eV and 486.75 eV to higher binding

energies of 495.61 eV and 487.15 eV after depositing SAMs on ITO (Fig. 1b). The In 3*d* XPS peak shifted from 444.75 eV and 452.31 eV of the ITO sample, to 445.22 eV and 452.72 eV after depositing SAMs on ITO substrate. The shifted binding energy verifies the assembled molecules onto the ITO substrate. Notably, the XPS peaks of Sn and In appeared at almost the same positions in all these SAM-modified ITO samples, indicating the similar molecular bonding on the ITO. This can be also confirmed through the DFT calculation (see calculation details in Supplementary Note 5). As shown in Supplementary Figs. 21 and 22, the comparative interaction energies between different SAMs and ITO indicate the similar anchoring behaviors of molecules with varied functional groups. This suggests the introduction of the functional groups shows negligible influence on the interaction of the carboxyl group with the ITO substrates.

To assess the influence of functional groups on molecular packing and stability, we conducted polarized Fourier-transform infrared (FTIR) spectroscopy before and after heating at 65 °C for 150 min to examine molecular stacking geometries and thermal stability. As shown in Supplementary Fig. 23, all four freshly prepared SAM layers exhibited a characteristic aromatic C–H stretching vibration mode around 3040 cm^{−1} with p-polarization, indicating that the conjugated pyrene core has a perpendicular component relative to the substrate. Additionally, vibration bands at around 2920 cm^{−1} and 2840 cm^{−1}, corresponding to C–H stretching in the tethering alkyl chain, were also observed with p-polarization. The perpendicular orientation of these probed bonds suggests that all four molecules adopt a vertical alignment, with their conjugated pyrene core group stacking in an in-plane ordered arrangement and the carboxylic acid anchoring group binding to the ITO surface^{11,23}. During the thermal ageing test, the signals corresponding to both the aromatic and alkyl C–H stretching vibrations remained largely unchanged, indicating that the molecular core group retained its original orientation. This highlights the exceptional structural rigidity conferred by the *peri*-fused polyaromatic core structure and confirms that the incorporation of functional groups has minimal impact on the stability of the SAM.

To evaluate the influence of the functional groups on perovskite crystallization, we performed X-ray diffraction (XRD) measurement on perovskite films based on different SAM layers (Fig. 2a). With almost no PbI₂ peak observed, the main diffraction peaks of each sample located at 14.1°, corresponding to the (100) planes. The peak position and the intensity of the XRD patterns of the perovskite films on different SAMs remained almost the same. Furthermore, 2-dimensional grazing-incidence wide-angle X-ray scattering (2D GIWAXS) was performed to study the perovskite orientation after depositing on different substrates. The GIWAXS patterns (Supplementary Fig. 24) along with integrated azimuth angle profiles of the (100) plane (Supplementary Fig. 25) demonstrate that the crystallographic orientation was also similar in these four cases. This evidence that the introduction of different functional groups did not significantly affect the crystallization and orientation of perovskite films. To study the surface morphology, scanning electron microscopy (SEM) was done. Figure 2b shows the SEM images of the surface of the as-deposited perovskite polycrystalline thin films, which showed similar morphology regardless of the introduction of different functional groups to the conjugation structure. The similar grain sizes and surface features confirm that the modification on SAM functional group would have negligible impact on the film quality of the perovskite layers deposited atop, which is consistent with the XRD results. We further evaluate the optical properties of the perovskite films using ultraviolet-visible (UV-vis) spectroscopy. The UV-vis spectra in Fig. 2c show that all perovskite films exhibited absorbance in the overall visible region with a threshold at approximately 738 nm, which is in accordance with the reported results²⁴. The similar shape and intensity of the absorption spectra indicate the light absorbance and optical bandgap of perovskite materials were not changed by the alteration of functional groups. We

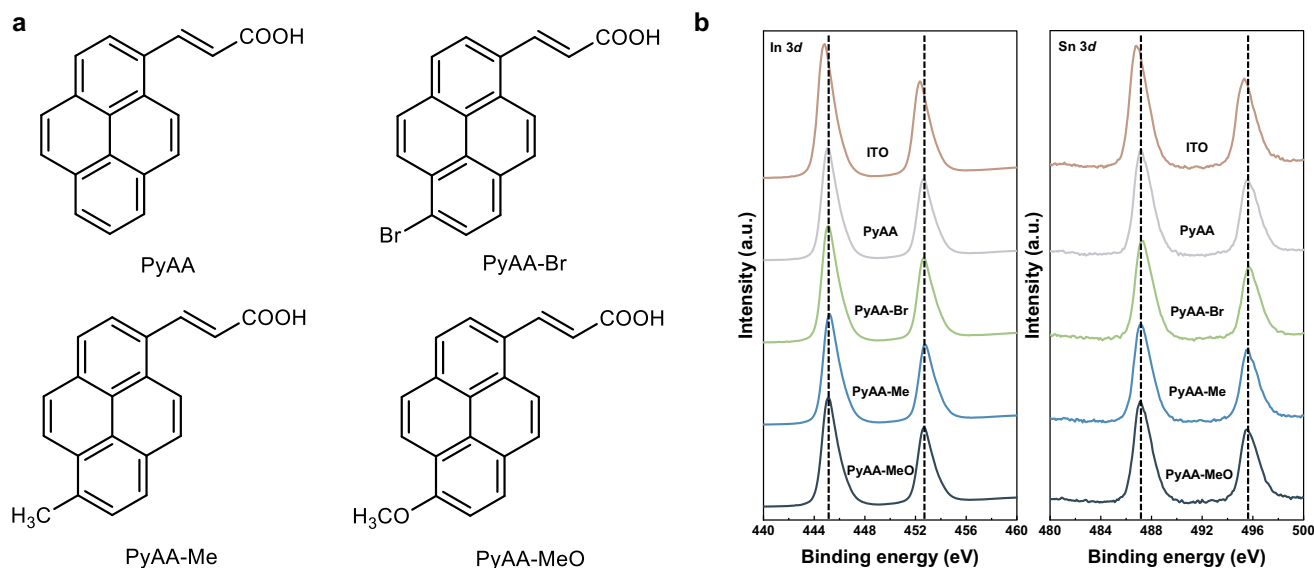


Fig. 1 | Molecular design and anchoring behavior. **a** Chemical structures of PyAA-Br, PyAA, PyAA-Me, and PyAA-MeO. **b** XPS of In 3d and Sn 3d for bare ITO substrate, and different SAMs deposited on the ITO.

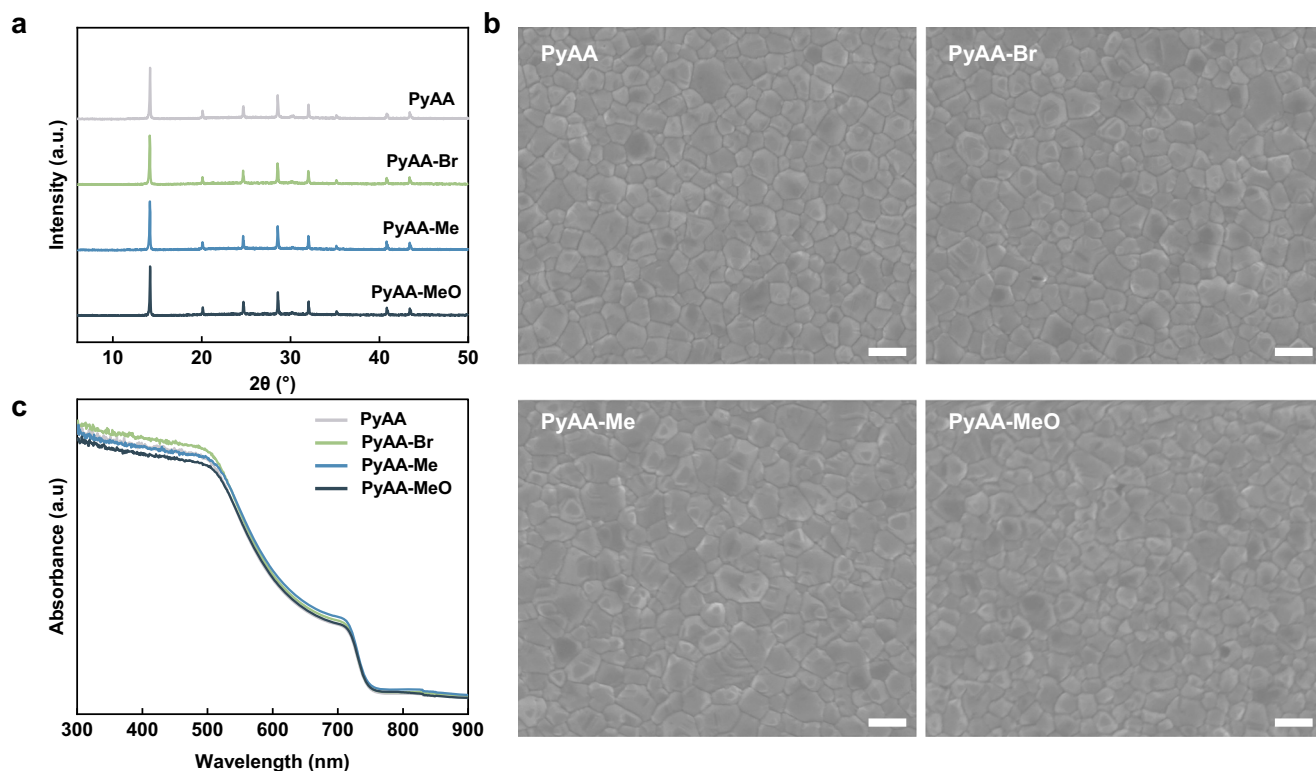


Fig. 2 | Properties of perovskite films. **a** XRD patterns of perovskite films on PyAA, PyAA-Br, PyAA-Me, PyAA-MeO, and ITO. **b** SEM images of perovskite films deposited on different SAMs. The scale bar is 400 nm. **c** UV-vis spectra of perovskite films deposited on different SAMs.

further evaluated the impact of SAM functional groups on the stability of wide-bandgap perovskites. To study the spectral photostability of the perovskite on different SAMs, we performed time-dependent in-situ photoluminescence (PL) emission spectroscopy on perovskite films based on different SAMs under continuous 520 nm laser radiation. The time-dependent PL spectra of the perovskites, collected over approximately 20 minutes of continuous irradiation, are shown in Supplementary Fig. 26. The PL spectra show that the initial emission peaks of the perovskite films with the four SAMs are all located at around 738 nm, suggesting that the SAM functional group has a minor

effect on the perovskite bandgap. This finding is consistent with the similar cutoff observed in the UV-vis spectra. After continuous illumination, all those PL peak positions shifted around 25 nm, and the width of each spectrum became larger. The similar behavior in terms of peak shift and peak broadening across the PL spectra for the four SAMs suggests that the phase segregation behavior of perovskite film is not significantly influenced by the functional group in the SAM layer. To further investigate the microscopic electronic properties of perovskite films on varied SAMs, we performed PL peak position mapping, as shown in Supplementary Fig. 27. The PL maps were collected for

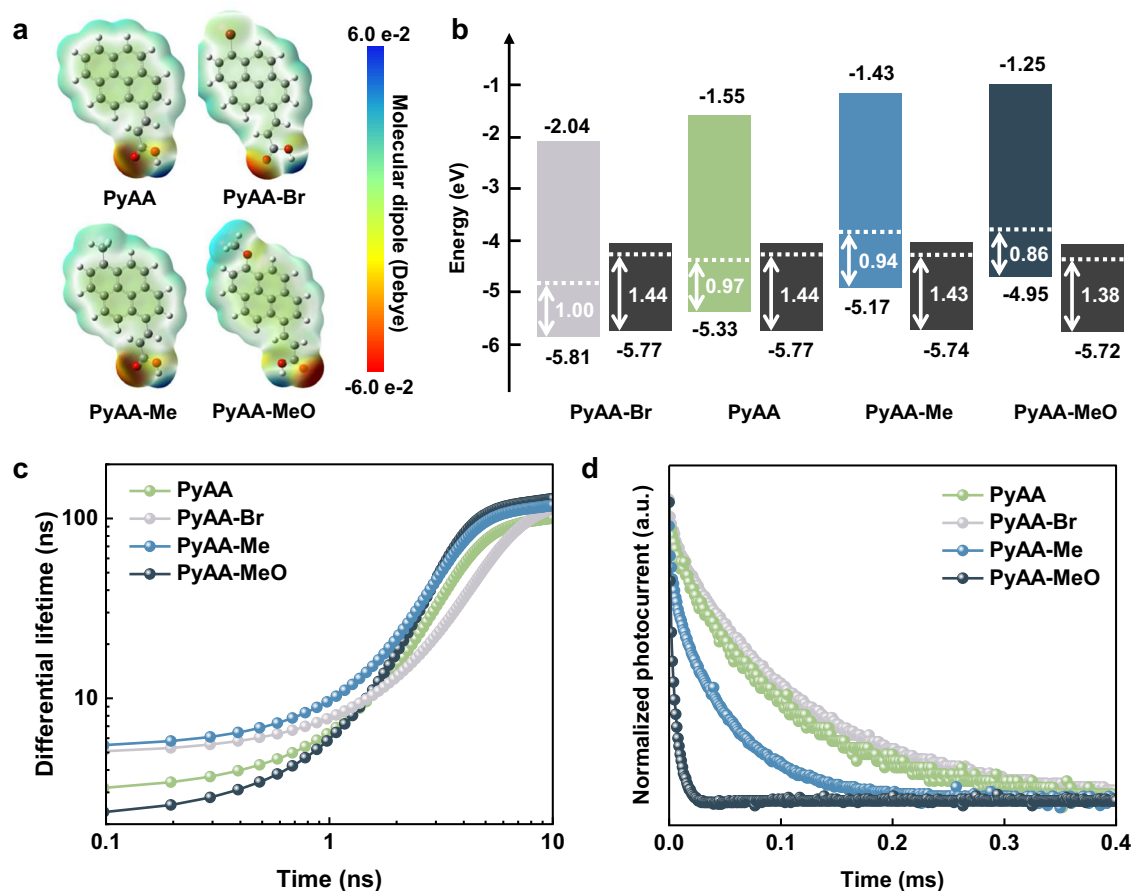


Fig. 3 | Enhanced hole extraction from improved energy alignment. **a** Calculated electron density of different SAMs using SCF methods. **b** Band structures of different SAMs and the corresponding perovskite films extracted from the UPS results. **c** Differential lifetime $\tau_{PL}(t)$ derived from TRPL measurements at a low laser

fluence of 2.6 nJ/cm^2 for perovskite films in contact with different SAMs. **d** Comparison of the TPC results of solar cell devices based on SAMs with varied functional groups.

before and after illumination under one-sun equivalent intensity for 24 h. The results reveal comparative red shift in PL emission across all four samples. This confirms that the functional groups in the SAMs have a negligible influence on the phase stability of wide-bandgap perovskite films. The above results together serve as a control to ensure the modification on functional groups showed negligible influence on the quality of the as-deposited perovskite films.

Inductive effect allowed for favored interfacial energetics

To study the influence of tethered functional groups on the surface electronic properties of the molecular-based contacts, we first performed Gaussian simulations to obtain the electrostatic potential (ESP, φ) of the four molecules (Fig. 3a). The minimum ESP (φ_{\min}) within each molecule, located on the functional group side, exhibits a decreasing trend from PyAA-Br to PyAA-MeO. This indicates that electron redistribution within molecules is influenced by the inductive effect induced by the substituents. Such inductive effect in turn modifies the molecular dipole moment. As obtained from the Gaussian simulation, the molecular dipoles for PyAA-Br, PyAA, PyAA-Me, and PyAA-MeO are 2.2, 3.6, 4.2, and 6.6 debyes, respectively. Consequently, the energy levels of molecular-based contacts can be precisely tuned in a stepwise manner over a defined range. After depositing the molecules as thin films on an ITO substrate, UV-vis measurements were conducted to determine the bandgap of each molecular thin film (Supplementary Fig. 28). The UV-vis spectra indicate that the bandgap of PyAA, PyAA-Br, PyAA-Me, and PyAA-MeO is 3.78, 3.77, 3.74, and 3.70 eV, respectively. Subsequently, ultraviolet photoelectron spectroscopy (UPS)

was performed to obtain the surface energy levels of the ITO modified with the SAMs (Supplementary Fig. 29). The Fermi levels (E_F) of the SAM layers were determined to be -4.81 , -4.36 , -4.23 , and -4.09 eV, with valence band maximum (VBM) of -5.81 , -5.78 , -5.30 , and -5.09 eV for PyAA-Br, PyAA, PyAA-Me, and PyAA-MeO, respectively. The smallest energy gap between the Fermi level and the VBM in PyAA-MeO indicates its strongest p-type character among the four SAMs. This finding can be corroborated by the Kelvin probe force microscope (KPFM) images (Supplementary Fig. 30), which reveal that the surface potential decreases with stronger electron-donating functional groups, demonstrating an increasingly pronounced p-type behavior from PyAA-Br to PyAA-MeO. Such p-type characteristic inherently promotes efficient hole extraction in perovskite solar cells. To further examine the energy alignment between SAM and perovskite, we utilized a copper deposition-assisted technique to peel off the perovskite layer from different SAMs²⁵ and performed UPS measurements on the exposed perovskite buried interface (Supplementary Fig. 31). The UPS results show that the energy level at the perovskite buried interface are similar across different substrates. Therefore, the observed improvement in energy alignment primarily stems from the modification in SAM energy levels. Figure 3b presents a schematic energy diagram of the four SAMs and the perovskite deposited on the respective substrates, referenced to the vacuum level. The offset between the Fermi level of the SAMs and that of the perovskite creates a built-in potential (V_{bi}), which provides the driving force for hole extraction. For PyAA-Br and PyAA, the deeper Fermi level of the SAMs compared to the perovskite results in an energy barrier for hole transfer. In contrast, the

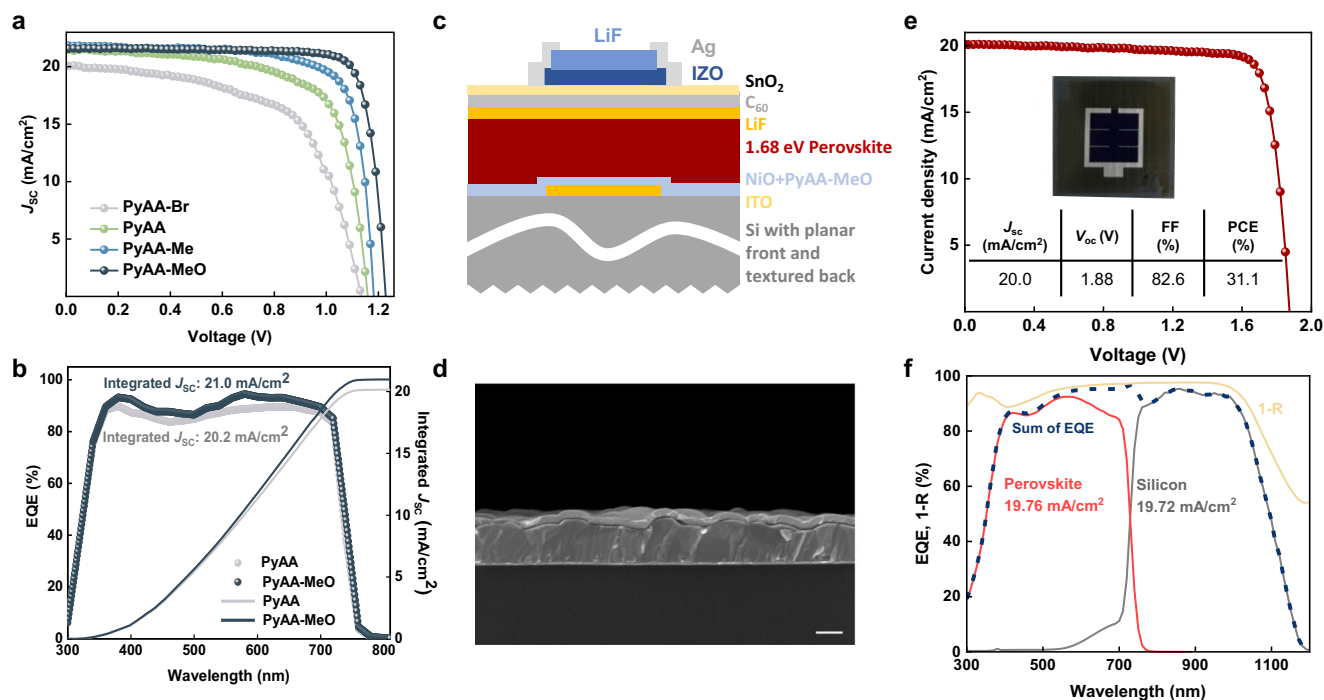


Fig. 4 | Photovoltaic performances. **a** J - V curves of the best-performing WBG perovskite solar cells based on different molecules. **b** EQE spectra of the best PyAA- and PyAA-MeO-based solar cell, with AM 1.5G-equivalent current densities given. **c** Schematic stack of the monolithic perovskite/silicon tandem solar cell. **d** Cross-

sectional SEM image of a perovskite/silicon tandem solar cell without the deposition of LiF and Ag. The scale bar is 400 nm. **e** J - V curve of the champion perovskite/tandem solar cell with an active area of 1 cm². **f** EQE spectra of a tandem device along with the sum of the EQE and the reflectance 1- R .

energy alignment at the SAM/perovskite interface for PyAA-Me and PyAA-MeO exhibits upward band bending, generating a driving force for hole extraction into the SAM layer. The energy offset is 0.08 eV for PyAA-Me and 0.25 eV for PyAA-MeO, demonstrating that PyAA-MeO provides the largest driving force for hole extraction among the four SAMs. Therefore, the inherent p-type characteristic of PyAA-MeO, combined with its largest driving force, significantly enhances hole extraction from the perovskite active layer.

To evaluate the influence of inductive effect on molecular hole extraction capability, we measured the time-resolved photoluminescence (TRPL) of perovskite films deposited on the different SAM layers under low laser fluence of 2.6 nJ/cm². The derived differential lifetimes are shown in Fig. 3c. The first interval in the differential lifetime profile of PyAA-MeO-based sample shortest among the four SAMs. This process is dominated by the charge transfer process, verifying the superior interfacial charge extraction of PyAA-MeO^{26,27}. Such a rapid hole extraction is facilitated by the inductive effect from the electron-donating methoxy group, leading to a more p-type molecular-based contact that is energetically favored with respect to the wide-bandgap perovskite. For SAM-incorporated devices, we further conducted transient photocurrent decay (TPC) measurements under the short-circuit condition to investigate the impact of the inductive effect on hole extraction. As shown in Fig. 3d, the PyAA-MeO-based device exhibited a fastest TPC decay compared to the other SAMs, suggesting enhanced hole extraction at the interface²⁸. Therefore, the introduction of the inductive effect enables the tuning of the SAM energy level over a specific range as needed. Among the four SAMs, the interfacial energetics between PyAA-MeO and the wide-bandgap perovskite is tuned to be the mostly favored, enabling the fastest hole extraction in the device.

Perovskite-based solar cell performances

Building on the virtues of inverted organic-inorganic PSCs, the 1.68 eV “triple cation” perovskite with the composition of

CS_{0.05}MA_{0.15}FA_{0.8}PbI_{2.25}Br_{0.75} was utilized in this study. Figure 4a shows the J - V characteristics under simulated AM 1.5 G illumination of the champion PSCs obtained on the respective SAMs in forward scan (J_{sc} to V_{oc}) and reverse scan (V_{oc} to J_{sc}) direction, with continuous maximum power point tracks (MPPT) provided in Supplementary Fig. 32. From the J - V curves, the hysteresis is overall negligible with MPP-tracked efficiencies close to the respective J - V scan values. Supplementary Fig. 33 summarized the statistical distribution of the PCE, fill factor (FF), J_{sc} , and V_{oc} of the devices based on different SAMs. It shows the average efficiency of devices based on different SAMs gradually enhanced from PyAA-Br (12.9%) to PyAA (16.6%) to PyAA-Me (19.1%) to PyAA-MeO (22.1%), with the main contribution stemming from the improved V_{oc} , FF, and J_{sc} . The photovoltaic parameters are summarized in Table 1. The champion device is based on PyAA-MeO, achieving a PCE of 22.8%, with a V_{oc} of 1.24 V, an FF of 84.3%, and a J_{sc} of 21.8 mA cm⁻². Considering the very similar crystallinity and light absorption of the perovskite layer, the performance gain should be mainly ascribed to the improved hole extraction at the perovskite/SAM interface, which stems from the favored interfacial energetics with the aid of inductive effect. The high V_{oc} and FF of PyAA-MeO-based devices reflect the low non-radiative recombination raised from the fast carrier extraction. To evaluate the V_{oc} loss in perovskite photovoltaic devices, we have performed photoluminescence quantum yield (PLQY) measurement on perovskite films based on different SAMs²⁹. As shown in Supplementary Fig. 34, the PLQY values under one-sun illumination are determined to be 0.70%, 3.96%, 4.17%, and 5.71% for PyAA-Br, PyAA, PyAA-Me, and PyAA-MeO, respectively. We also quantified the energy loss of perovskite films on different SAMs by analyzing quasi-Fermi level splitting (QFLS) enhancement, derived from the PLQY results (Supplementary Fig. 35)³⁰. Compared with the PyAA-Br sample, the QFLS enhancement increases from 17.2 to 48.1 meV as the electron-donating effect of the functional group becomes stronger. The largest QFLS enhancement in the PyAA-MeO-incorporated perovskite

Table 1 | Photovoltaic parameters from *J*-*V* scans under illumination in forward scan direction of base PSCs based on different investigated SAMs

SAM	J_{SC} (mA cm ⁻²)	V_{OC} (V)	FF (%)	PCE (%)
PyAA	21.5	1.16	69.1	17.2
PyAA-Br	20.3	1.13	60.1	13.8
PyAA-Me	21.9	1.18	76.4	19.7
PyAA-MeO	21.8	1.24	84.3	22.8

film which aligns well with the highest V_{OC} observed in the photovoltaic devices. For further verification, we measured the external quantum efficiency of electroluminescence (EQE_{EL}) based on full devices. As shown in Supplementary Fig. 36, the EQE_{EL} value increases as the electron-donating effect from the functional group become stronger. This results in the minimal ΔV of 0.18 mV in PyAA-MeO. This is attributed to the favorable interfacial energy alignment, which facilitates efficient hole extraction and reduces charge accumulation and recombination at the interface. Figure 4b displays the external quantum efficiencies (EQE) of the champion devices based on PyAA (20.2 mA cm⁻²) and PyAA-MeO (21.0 mA cm⁻²), respectively. The increased current density from EQE integration can be attributed to the more efficient hole extraction stemming from the improved energy alignment. To further demonstrate the potential application of the PyAA-MeO, we integrated the optimized WBG PSCs with the commercialized TOPCon c-Si subcells. The NiO_x layer was used in the tandem devices to achieve better device performance. Using Si wafer with a planar front and a textured back, a schematic stack of the perovskite/TOPCon tandem solar cells is shown in Fig. 4c, with a cross-sectional SEM image of a part of the tandem solar cell displayed in Fig. 4d. As shown in Fig. 4e, a champion efficiency of 31.1% (certified 30.91%, see the certificate in Supplementary Fig. 37) was achieved for the best-performing centimeter-scale perovskite/TOPCon tandem solar cells, with a high FF of 82.6%, a V_{OC} of 1.88 V, and a J_{SC} of 20.0 mA cm⁻², which stands as one of the highest reported TOPCon tandems to date (Supplementary Table. 1). Stabilized output efficiencies of 31.1% is provided in Supplementary Fig. 38. The EQE-integrated J_{SC} values for WBG and silicon subcells measured from a perovskite/silicon tandem photovoltaic device are 19.8 mA cm⁻² and 19.7 mA cm⁻², respectively (Fig. 4f). This demonstrated the reliability and potential application of the inductive effect modification strategy for wide-bandgap perovskite solar cells.

In addition to the improved PCE, an enhanced stability was also observed for PyAA-MeO-based PSCs. According to the International Summit on Organic Photovoltaic Stability (ISOS) protocols, the time-dependent PCEs of devices were tracked under accelerated-aging conditions. The maximum power point tracking (MPPT) for unencapsulated devices under simulated 1 sun AM 1.5 G illumination is shown in Supplementary Fig. 39 (initial photovoltaic parameters for MPPT devices are provided in Supplementary Table. 2). MPPT was done without active sample cooling, where the operating temperature of the samples reaches 60 °C. We compared the stability of PyAA- and PyAA-MeO-based devices with a conventional hole transporting material (2-(9H-carbazol-9-yl)ethyl)phosphonic acid (2PACz, see the *J*-*V* curve of the champion device and the statistical distribution of the PCE, V_{OC} , FF, and J_{SC} of the devices based on 2PACz in Supplementary Fig. 40 and Fig. 41). While 2PACz-based devices retained only 84% of their initial PCE, both PyAA and PyAA-MeO-based devices exhibit superior stability. PyAA-MeO-based devices showed minimal changes, retaining over 99% of its initial PCE after 400 h, with a linear extrapolation to a T80 of 15334 h (T80 means the time for a PSC to degrade to 80% of its initial PCE). To test the light stability, the devices were aged under

continuous 1-sun illumination under open-circuit conditions according to the ISOS-L-1 protocol. The device with PyAA-MeO retained about 96% of its initial PCE after more than 2400 h (Supplementary Fig. 42). To evaluate the thermal stability, the devices were continuously heated at 65 °C following the ISOS-D-2 protocol. The PCE of 2PACz-based devices decays swiftly over time, both PyAA and PyAA-MeO exhibited outstanding device stability, with PyAA-MeO-based devices retaining over 98% of its initial PCE after more than 2400 h (Supplementary Fig. 43). These results indicate the modification on the molecule functional group does not compromise the device stability.

Discussion

We have designed and synthesized SAMs to specifically cater to wide-bandgap perovskite via precisely tuning their energy level with the aid of inductive effect. By introducing electron-withdrawing or -donating functional groups, the inductive effect from the substituents allows the redistribution of electron clouds, which modifies the energy level of molecules. The PyAA-MeO, a SAM based on electron-donating methoxy group, constructs a p-type HTL in contact with the perovskite on top. The favored interfacial energetics improve the hole extraction on the HTL/perovskite interface and exhibit exceptional stability. The results highlight the possibility of the rational design of SAMs by making use of the inductive effect to achieve favored interfacial energetics with wide-bandgap perovskite. We believe this strategy is promising in contributing to the commercialization of perovskite and perovskite/TOPCon tandem solar cells.

Methods

Materials

All materials used in this work were obtained commercially and used without further purification unless otherwise specified. The transparent indium tin oxide glass (ITO, 10 Ω per square, transmittance 88%) was purchased from Shenzhen Huayu United Technology Co., Ltd. The TOPCon silicon substrate was provided by Jietai New Energy Technology Co., Ltd. The perovskite raw materials including lead iodide (PbI₂, purity 99.999%, perovskite grade), formamidinium iodide (FAI, purity 99.99%), methylammonium bromide (MABr, purity 99.9%), lead bromine (PbBr₂, purity 99.9%), lithium fluoride (LiF, purity 99.99%) and C60 (purity 99.9%) were all purchased from Advanced Election Technology Co., Ltd. Bathocuproine (BCP, purity 99%), cesium iodide (CsI, purity 99.999%) and oleylammonium iodide (OAI, purity 99.5%) were purchased from Xi'an Yuri Solar Co., Ltd. [2-(9H-carbazol-9-yl) ethyl] phosphonic acid (2PACz, purity 98%) was obtained from Tokyo Chemical Industry Co., Ltd. The required solvent including N, N-Dimethylformamide (DMF, extra dry, purity 99.8%), isopropanol (IPA, extra dry, purity 99.8%), ethanol (extra dry, purity 99.8%), and chlorobenzene (CB, extra dry, purity 99.5%) were purchased from J&K Scientific. Dimethyl sulfoxide (DMSO, anhydrous, ≥99.9%) and silver (Ag, purity 99.99%) were purchased from Sigma-Aldrich Inc. All chemical reagents were used as received without further purification unless otherwise specified.

Preparation of molecule precursors and films

For the preparation of molecule solutions, the 2PACz and the home-synthesized PyAA, PyAA-Br, PyAA-Me, and PyAA-MeO molecule powders were fully dissolved at a concentration of 2 mM into a mixed solvent of ethanol and DMF at volume ratio 3:1 at room temperature. The molecule solutions were stirred overnight in nitrogen glove box. To prepare the films, the filtered molecule solutions were spin-coated at 1000 rpm for 10 s and 3000 rpm for 40 s in the nitrogen glovebox. Afterwards, the films were annealed at 115 °C for 20 min.

Preparation of perovskite precursors and films

For the preparation of perovskite films with a composition Cs_{0.05}MA_{0.15}FA_{0.8}PbI_{2.25}Br_{0.75}, 1.65 M perovskite precursor solution

was prepared by dissolving CsI, FAI, MABr, PbBr₂ and PbI₂ in 1 mL mixed solvent of DMF and DMSO at volume ratio 4:1. Additional 5 mol% PbI₂ was added to the precursor solution and the solution was stirred overnight. The filtered perovskite precursor was then spin-coated on substrate at 1000 rpm for 10 s and 5000 rpm for 40 s in nitrogen glovebox. 250 μ L of CB anti-solvent was dropped quickly at 25 s during the second spinning step. Afterwards, the film was annealed at 110 °C for 30 min.

Fabrication of inverted perovskite solar cell devices

The pre-patterned ITO glasses (15 mm \times 15 mm) were washed with detergent solution, deionized water, acetone, and isopropanol (IPA), each under 30 minutes of sonication, followed by drying with a pure nitrogen flow. The cleaned and dried ITO substrates were then treated with ultraviolet-ozone for 30 min before transferred into glovebox filled with nitrogen. The molecule solution was spin-coated onto the ITO substrates following the abovementioned method. After cooling down to room temperature, perovskite films were coated on these layers following the abovementioned method. For the surface passivation layer, OAml was dissolved in IPA with a concentration of 0.5 mg mL⁻¹ and stirred at room temperature for 2 h. The OAml solution was spin-coated on top of the as-prepared perovskite at 5000 rpm for 30 s, and then transferred to the hotplate and annealed at 100 °C for 5 min.

After cooling down to room-temperature, the whole device was transferred to a vacuum chamber under a base pressure of $<5.0 \times 10^{-6}$ Pa. 1.0 nm LiF at a rate of 0.1 \AA s^{-1} , 30 nm C60 at a rate of 0.3 \AA s^{-1} and 8 nm BCP at a rate of 0.2 \AA s^{-1} were thermally evaporated on the perovskite thin film sequentially (Angstrom Engineering Inc) respectively, without breaking vacuum. Finally, 100 nm thick Ag electrode at a rate of 1.5 \AA s^{-1} was deposited to complete the devices for current density-voltage (*J-V*) measurements or stability tests.

Fabrication of tandem solar cell devices

The Si bottom wafers with a 20 nm ITO recombination layer were subjected to UV-Ozone treatment for 20 min. Then the substrate was spin-coated with a thin layer of NiO_x nanoparticle film (10 mg mL⁻¹ NiO_x water solution) at 3000 rpm for 30 s, and annealed in ambient air at 120 °C for 20 min, and then transferred into glovebox filled with nitrogen. The molecule solution was spin-coated onto the ITO/Si substrates following the abovementioned method. After cooling down to room temperature, perovskite films and the surface passivation layer were coated on these layers following the abovementioned method. After that, -1 nm LiF and 20 nm C60 were deposited by thermal evaporation. And then 20 nm SnO₂ was then deposited by atomic layer deposition (ALD) using a Veeco system. The substrate temperature was maintained at 85 °C during ALD deposition with TDMASn precursor source at 60 °C. The pulse and purge time for Tetrakis(dimethylamino)tin(IV) (TDMASn) is 1 and 10 s with a 90 sccm carrier gas of nitrogen, for H₂O is 0.15 and 10 s with 90 sccm N₂. 180 cycles were used. 80 nm IZO was sputtered from a 3-inch IZO ceramic target on top of the SnO₂ through a shadow mask. Ag finger with a thickness of 250 nm was thermally evaporated using a high precision shadow mask. Finally, 100 nm LiF was thermally evaporated as an anti-reflection layer.

Exfoliation of perovskite films

A metal encapsulation method, previously reported in our work, was employed for perovskite exfoliation. Initially, a Ti (50 nm)/Cu (3 μ m) bilayer structure is deposited onto the perovskite using magnetron sputtering. The Ti layer serves to enhance adhesion between the Cu and perovskite, while the Cu layer acts as a stressor, facilitating the initiation of fracture at the interface between the perovskite and the substrate. After Cu deposition, the sample is adhered to a rigid substrate, such as Si, using double-sided tape. The role of this substrate is

to maintain the perovskite's flatness and to support the exfoliation process. Following this, the perovskite layer can be peeled off.

Device characterization

J-V characteristics of photovoltaic cells were taken using a Keithley 2400 source measure unit under a simulated AM 1.5 G spectrum, with an Oriel 9600 solar simulator. The illumination light was calibrated to 100 mW cm⁻² AM 1.5 G using a silicon reference cell. Typically, the devices were measured in reverse scan (1.25 V \rightarrow 0 V, step 0.02 V). All the devices were measured without pre-conditioning such as light-soaking, and applied a bias voltage. Steady-state power conversion efficiency was calculated by measuring stabilized photocurrent density under a constant bias voltage. External quantum efficiencies (EQEs) were measured using an integrated system (Enlitech) and a lock-in amplifier with a current preamplifier under short-circuits' conditions. Transient photocurrent (TPC) decay under the short-circuit condition was conducted by Photo-Electrochemical measurement system of Zahner CIMPS-abs. The transient photo intensity applied was 500 mW cm⁻². The applied voltage of 0.5 V was used.

Device stability test

The devices for stability test were fabricated using the method mentioned above with a structure of ITO/SAM/perovskite/C60/BCP/Ag. The thickness of C60 layer was 100 nm. To measure the light stability of the unencapsulated devices, we stored devices under AM1.5 illumination (100 mW cm⁻²) in N₂ environment. The thermal stability of unencapsulated inverted PSCs was performed under 65 °C heating in N₂ environment. The operational stability tests were carried out at the maximum power point (MPP) under AM1.5 illumination (100 mW cm⁻²) in ambient air at -60 °C. The voltage at the MPP was automatically applied, and the power output of the devices was tracked.

Materials characterizations

NMR spectra was recorded on an Agilent DD2 400 MHz spectrometer or Bruker Advance 600 MHz in deuterated solvents (400 or 600 MHz for ¹H and 101 or 151 MHz for ¹³C). Chemical shifts in ¹H NMR spectra are reported in ppm on the δ scale from an internal standard of TMS. Data are reported as follows: chemical shift, multiplicity (s = singlet, d = doublet, t = triplet, q = quartet, m = multiplet, br = broad peak), coupling constant in hertz (Hz), and integration. Chemical shifts of ¹³C{¹H} NMR spectra are reported in ppm from the central peak of deuterated solvents on the δ scale. High resolution mass spectrometry (HRMS) was performed on Bruker UHR-TOF maXis and is reported as *m/z*. Infrared spectrometry (IR) was performed on Bruker Tensor 27 and is reported as cm⁻¹. UV-vis absorption spectra of the perovskite films and ITO glass were obtained using a Shimadzu UV-VIS-NIR (UV3600Plus + UV2700) equipped with integrating sphere, in which monochromatic light was incident to the substrate side. UPS measurements were carried out to determine the work function and the position of valence band maximum of materials. A He discharge lamp, emitting ultraviolet energy at 21.2 eV, was used for excitation. All UPS measurements were performed using standard procedures with a -10 V bias applied between the samples and detectors. Clean gold was used as a reference. High-resolution X-ray photoelectron spectroscopy (XPS) measurements were carried out on an XPS (ThermoFisher ESCALAB Xi +). An Al K α (1486.6 eV) X-ray was used as the excitation source. X-ray diffraction (XRD) characterization was carried out on a D2 Phaser instrument with a Cu K α (λ = 0.154 \AA) radiation, equipped with 1D LynxEye detector. SEM was carried out on the Field Emission Environment Scanning Electron Microscope of QuattroS. The time-resolved photoluminescence spectra were obtained by Edinburgh FLS980 applied with an excitation wavelength of 485 nm. The Jupiter XR Oxford Instruments were used for the KPFM measurements of the molecular films. TGA curves were measured on a Mettler-Toledo

TGA/DSC 3+/1600 HT. The Temperature range was set to be 30–800 °C, with a step of 5 °C/min. PLQY values of perovskite films were collected by a fibre-coupled spectrometer, paired with a 405 nm power-tunable CW laser to photoexcite the films within an integrating sphere. The power of the excitation light is precisely measured utilizing a calibrated power meter. The Quasi-Fermi level splitting (QFLS) values of 1.68 eV bandgap perovskite films on different HSLs on the ITO substrate were obtained by using PLQY measurements using the following equation⁶:

$$QFLS = QFLS_{rad} + k_B T \cdot \ln(PLQY) = k_B T \cdot \ln\left(PLQY \frac{J_G}{J_{0,rad}}\right) \quad (1)$$

Where k_B is the Boltzmann constant, and T is the temperature. J_G is the generation current density under illumination, in this case, approximated to the short-circuit current density J_{SC} of devices. $J_{0,rad}$ is the dark radiative recombination saturation current density. According to the detailed balance under open-circuit conditions, $J_{0,rad}$ can be obtained by the following equations:

$$J_{0,rad} = e \int_0^\infty EQE_{PV}(E) \Phi_{BB}(E) dE \quad (2)$$

$$\Phi_{BB}(E) = \frac{2\pi E^2}{h^3 c^2} \cdot \frac{1}{\exp\left(\frac{E}{k_B T}\right) - 1} \quad (3)$$

EQE_{EL} values of perovskite films were collected by a commercialized system (LQE-50X-EL, Enlitech) that was equipped with an integrated sphere and a photomultiplier tube. For the polarized FTIR measurements, 30-nm ITO was first deposited on 2-mm-thick Al_2O_3 substrates with d.c. magnetron sputter deposition at room temperature. To deposit the SAM layers on the Al_2O_3 /ITO substrates, the SAM solutions with 2 mM in mixed solvent of ethanol and DMF at volume ratio 3:1 was spin-coated 1000 rpm for 10 s and 3000 rpm for 40 s in the nitrogen glovebox. Afterwards, the films were annealed at 115 °C for 20 min as fresh films. For the assessment of the aged samples, the fresh films were further heated at 65 °C for 150 min before measurements. The polarized FTIR spectra were captured at room temperature with an FTIR spectrometer (Thermo Fisher Nicolet IS50) equipped with a MCT detector. The polarizer is made of ZnSe, which limits the low-end spectral range to around 650 cm^{-1} . The spectral resolution was set to 4 cm^{-1} , the aperture was set to 4 mm, and spectra were acquired by averaging 64 scans. Grazing-incidence wide-angle X-ray scattering (GIWAXS) measurement for perovskite films was conducted at 298 K, performed on a Bruker D8 Venture diffractometer, equipped with a metal-jet microfocus source (Ga K α radiation, $\lambda = 1.34138 \text{ \AA}$), PHOTON III detector in shutterless mode, and Oxford 1000 Plus cryosystem. The integration of frames was processed by APEX 4 software package. For the time-resolved photoluminescence (TRPL) spectroscopy measurements, the sample was excited with a picosecond pulsed diode laser (Pico-quant LDH 450), with a 70-ps pulse width and 20 MHz repetition rate, focused on sample with a $\times 100$ objective (numerical aperture 0.90). The photoluminescence signal was acquired through the TCSPC strobeflock system. The energy density of laser for TRPL measurements was set to be 2.6 nJ cm^{-2} . The total instrument response function for the photoluminescence decay was less than 200 ps, and the temporal resolution was less than 30 ps. Contact angle measurements were done with high precision ($\pm 0.1^\circ$ accuracy) using a CA200 contact angle analyzer. The in-situ photoluminescence emission spectroscopy and PL mapping were collected on Alpha300RAS (WITec GMBH, Germany) Raman system. A diode-pumped solid-state laser (532 nm, cobalt Laser) was focused on sample with a diffraction-limited beam size of 900 nm by a long working distance 50X Zeiss LD EC Epiplan-Neofluar

Dic objective (NA = 0.55). A G2 grating (600 g mm^{-1} , BLZ = 500 nm) was used.

Reporting summary

Further information on research design is available in the Nature Portfolio Reporting Summary linked to this article.

Data availability

All the data needed to evaluate the conclusions in the paper are present in the paper or Supplementary Information. The atomic coordinate of the optimized computational models are provided in Supplementary Data 1–4. Source data are provided with this paper.

References

- Mariotti, S. et al. Interface engineering for high-performance, triple-halide perovskite-silicon tandem solar cells. *Science* **381**, 63–69 (2023).
- Chin, X. Y. et al. Interface passivation for 31.25%-efficient perovskite/silicon tandem solar cells. *Science* **381**, 59–63 (2023).
- Tong, J. et al. Wide-bandgap metal halide perovskites for tandem solar cells. *ACS Energy Lett.* **6**, 232–248 (2020).
- Koopmans, M. & Koster, L. J. A. Voltage deficit in wide bandgap perovskite solar cells: the role of traps, band energies, and effective density of states. *Sol. RRL* **6**, 2200560 (2022).
- Oliver, R. D. J. et al. Understanding and suppressing non-radiative losses in methylammonium-free wide-bandgap perovskite solar cells. *Energy Environ. Sci.* **15**, 714–726 (2022).
- Stolterfoht, M. et al. The impact of energy alignment and interfacial recombination on the internal and external open-circuit voltage of perovskite solar cells. *Energy Environ. Sci.* **12**, 2778–2788 (2019).
- Zhang, S. et al. Minimizing buried interfacial defects for efficient inverted perovskite solar cells. *Science* **380**, 404–409 (2023).
- Al-Ashouri, A. et al. Monolithic perovskite/silicon tandem solar cell with >29% efficiency by enhanced hole extraction. *Science* **370**, 1300–1309 (2020).
- He, R. et al. All-perovskite tandem 1- cm^2 cells with improved interface quality. *Nature* **618**, 80–86 (2023).
- Zhen, L. et al. Stabilized hole-selective layer for high-performance inverted p-i-n perovskite solar cells. *Science* **382**, 284–289 (2023).
- Al-Ashouri, A. et al. Conformal monolayer contacts with lossless interfaces for perovskite single junction and monolithic tandem solar cells. *Energy Environ. Sci.* **12**, 3356–3369 (2019).
- Wu, X. et al. Backbone engineering enables highly efficient polymer hole-transporting materials for inverted perovskite solar cells. *Adv. Mater.* **35**, e2208431 (2023).
- Aktas, E. et al. Understanding the perovskite/self-assembled selective contact interface for ultra-stable and highly efficient p-i-n perovskite solar cells. *Energy Environ. Sci.* **14**, 3976–3985 (2021).
- Ullah, A. et al. Versatile hole selective molecules containing a series of heteroatoms as self-assembled monolayers for efficient p-i-n perovskite and organic solar cells. *Adv. Func. Mater.* **32**, 2208793 (2022).
- Chieh-Ming, H. et al. Self-assembled monolayers of bi-functionalized porphyrins: a novel class of hole-layer-coordinating perovskites and indium tin oxide in inverted solar cells. *Angew. Chem. Int. Ed.* **62**, e202309831 (2023).
- Wu, Y. Neglected acidity pitfall: boric acid-anchoring hole-selective contact for perovskite solar cells. *Natl Sci. Rev.* **10**, nwad057 (2023).
- Chieh-Ming, H. et al. Repairing interfacial defects in self-assembled monolayers for high-efficiency perovskite solar cells and organic photovoltaics through the sam@pseudo-planar monolayer strategy. *Adv. Sci.* **11**, 2404725 (2024).
- Arkan, E. et al. Effect of functional groups of self assembled monolayer molecules on the performance of inverted perovskite solar cell. *Mater. Chem. Phys.* **254**, 123435 (2020).

19. Zixuan, H. et al. Highly efficient blade-coated 1.67 eV p-i-n perovskite solar cells enabled by a hybrid self-assembled monolayer and surface passivation. *ACS Appl. Energy Mater.* **7**, 11683–11690 (2024).
20. Zhao, K. et al. *peri*-Fused polyaromatic molecular contacts for perovskite solar cells. *Nature* **632**, 301–304 (2024).
21. Daley, R. *Organic Chemistry*, Part 1 of 3 56–57 (Lulu Press, Morrisville, 2005).
22. Stock, L. The origin of the inductive effect. *J. Chem. Educ.* **49**, 400 (1972).
23. Truong, M. A. et al. Tripodal triazatruxene derivative as a face-on oriented hole-collecting monolayer for efficient and stable inverted perovskite solar cells. *J. Am. Chem. Soc.* **145**, 7528–7539 (2023).
24. Hou, Y. et al. Efficient tandem solar cells with solution-processed perovskite on textured crystalline silicon. *Science* **6**, 1135–1140 (2020).
25. Sun, X. et al. In-plane compressive strain stabilized formamidinium-based perovskite. *Matter* **8**, 101920 (2025).
26. Krogmeier, B. et al. Quantitative analysis of the transient photoluminescence of CH₃NH₃PbI₃/PC61BM heterojunctions by numerical simulations. *Sustain. Energy Fuels* **2**, 1027–1034 (2018).
27. Krückemeier, L. et al. Understanding transient photoluminescence in halide perovskite layer stacks and solar cells. *Adv. Energy Mater.* **11**, 2003489 (2021).
28. Zhu, J. et al. A donor–acceptor-type hole-selective contact reducing non-radiative recombination losses in both subcells towards efficient all-perovskite tandems. *Nat. Energy* **8**, 714–724 (2023).
29. Cheng, Z. et al. Interfacial and permeating modification effect of n-type non-fullerene acceptors toward high-performance perovskite solar cells. *ACS Appl. Mater. Interfaces* **13**, 40778–40787 (2021).
30. Liu, S. et al. Buried interface molecular hybrid for inverted perovskite solar cells. *Nature* **632**, 536–542 (2024).

Acknowledgements

All the authors thank L. Liu, Y. Nie from Instrumentation and Service Center for Physical Sciences (ISCPs), Z. Chen and Y. Cheng from Instrumentation and Service Center for Molecular Sciences at Westlake University for the assistance in the characterizations. J.X. acknowledge grants (grant numbers LR24F040001, LDG25E020001 and LD24E020001) from the Natural Science Foundation of Zhejiang Province of China, the grant from the National Natural Science Foundation of China (grant number 62274146), the support from the Fundamental Research Funds for the Central Universities (226-2022-00200), the grant from the Research and Development Foundation of Dongfang Electric (Hangzhou) Innovation Institute Co., Ltd. (grant number 4F-CSC24005), and Zhejiang Province's Vanguard and Leader Geese Research and Development Program (2024C01246(SD2)). R.W. acknowledges a grant from the National Natural Science Foundation of China (grant number 62474143) and support from the Key R&D Program of Zhejiang (2024SSYS0061). This work was also supported by the Zhejiang Key Laboratory of Low-Carbon Intelligent Synthetic Biology (2024ZY01025) and Muyuan Laboratory (programme ID 14136022401). Z.C. acknowledges the grant by the National Natural Science Foundation of China

(Grant No. 62204220). Y.T. acknowledges the grant by the National Natural Science Foundation of China (Grant No. 624B2117).

Author contributions

J.X., Y.L., and Y.T. conceived the idea. Y.L. and Y.T. did the fabrication of perovskite photovoltaic devices and the data analysis under the supervision of D.Y. and J.X. C.L. synthesized the molecules under the supervision of R.L., K.Z., J.S., Z.C., C.D., X.S., L.Y., X.Z., P.S., and D.J. assisted with the characterizations and device fabrication. W.M., J.D., and M.T. assisted with fabricating the TOPCon subcells. C. D. and I. Y. conducted theoretical simulations. X.M. was responsible for the GIWAXS testing. Z.Z., N.D., and R.W. provide helpful discussions. Y.L. wrote the manuscript. All the authors discussed the results and commented on the manuscript.

Competing interests

The authors declare no competing interests.

Additional information

Supplementary information The online version contains supplementary material available at <https://doi.org/10.1038/s41467-025-59896-8>.

Correspondence and requests for materials should be addressed to Deren Yang or Jingjing Xue.

Peer review information *Nature Communications* thanks Hsieh-Chih Chen, and the other, anonymous, reviewer(s) for their contribution to the peer review of this work. A peer review file is available.

Reprints and permissions information is available at <http://www.nature.com/reprints>

Publisher's note Springer Nature remains neutral with regard to jurisdictional claims in published maps and institutional affiliations.

Open Access This article is licensed under a Creative Commons Attribution-NonCommercial-NoDerivatives 4.0 International License, which permits any non-commercial use, sharing, distribution and reproduction in any medium or format, as long as you give appropriate credit to the original author(s) and the source, provide a link to the Creative Commons licence, and indicate if you modified the licensed material. You do not have permission under this licence to share adapted material derived from this article or parts of it. The images or other third party material in this article are included in the article's Creative Commons licence, unless indicated otherwise in a credit line to the material. If material is not included in the article's Creative Commons licence and your intended use is not permitted by statutory regulation or exceeds the permitted use, you will need to obtain permission directly from the copyright holder. To view a copy of this licence, visit <http://creativecommons.org/licenses/by-nc-nd/4.0/>.

© The Author(s) 2025